# Experimental Demonstration of a Resonator-Induced Phase Gate in a Multiqubit Circuit-QED System

Hanhee Paik,[1,*] A. Mezzacapo,[1] Martin Sandberg,[1] D. T. McClure,[1] B. Abdo,[1] A. D. Córcoles,[1] O. Dial,[1] D. F. Bogorin,[2] B. L. T. Plourde,[2] M. Steffen,[1] A. W. Cross,[1] J. M. Gambetta,[1] and Jerry M. Chow[1]
[1]IBM T. J. Watson Research Center, Yorktown Heights, New York 10598-0218, USA
[2]Department of Physics, Syracuse University, Syracuse, New York 13244-1130, USA
(Received 6 June 2016; published 13 December 2016)

The resonator-induced phase (RIP) gate is an all-microwave multiqubit entangling gate that allows a high degree of flexibility in qubit frequencies, making it attractive for quantum operations in large-scale architectures. We experimentally realize the RIP gate with four superconducting qubits in a three-dimensional circuit-QED architecture, demonstrating high-fidelity controlled-Z (CZ) gates between all possible pairs of qubits from two different 4-qubit devices in pair subspaces. These qubits are arranged within a wide range of frequency detunings, up to as large as 1.8 GHz. We further show a dynamical multiqubit refocusing scheme in order to isolate out 2-qubit interactions, and combine them to generate a 4-qubit Greenberger-Horne-Zeilinger state.

DOI: 10.1103/PhysRevLett.117.250502

As recent progress in superconducting quantum processors has marched towards more complex networks of qubits [1–3], it becomes increasingly crucial to develop robust protocols for multiqubit control. In particular, there has been a considerable amount of work on improving single- [4] and 2-qubit [5–7] controls for superconducting qubits. Although the fidelity of single-qubit gates (>0.999) has already been pushed above fault-tolerant thresholds for error correction codes such as the surface code [8,9], the study of 2-qubit gates in multiqubit systems is still an area of great exploration.

Currently, many 2-qubit gates for superconducting qubits require specific arrangements of qubit frequencies to perform optimally. For example, the dynamically tuned controlled-Z (CZ) gate [5,10,11] functions through frequency tuning two qubits into a specific resonance condition involving higher energy levels, which will not work if any other existing energy levels intervene between the qubits. A similar limitation arises with the all-microwave cross-resonance (CR) gate [6,12–14]. The CR gate works for qubits within a narrow window of detunings defined by the anharmonicity of the qubit [15]. This restriction becomes accentuated in larger networks of qubits where all qubit frequencies must be arranged within a small frequency window [16].

A notable advantage of the resonator-induced phase (RIP) gate [17,18] is its capability to couple qubits even if they are far detuned from each other. Therefore, the RIP gate can overcome difficulties due to constraints on the frequency arrangements that can hinder scalability towards larger quantum architectures. The RIP gate is a CZ gate that exploits strong coupling between qubits and a resonator in a circuit quantum electrodynamics (cQED) system. It is realized by applying a detuned microwave pulse to a shared bus cavity, without a strong requirement on the qubit frequencies. In addition, it is insensitive to phase fluctuations of the drive, depending only on drive amplitude and detuning.

In this Letter, we experimentally demonstrate the RIP gate in two cQED devices, each composed of four three-dimensional transmon superconducting qubits [19] coupled to both a central bus cavity and individual readout cavities. First, we show that a variety of state-dependent phases are induced by the RIP gate. Phases from weight two and three Pauli operators are singled out using echo sequences. Our experiments confirm the predicted dependence of the acquired phases on drive amplitude and detuning. Then,

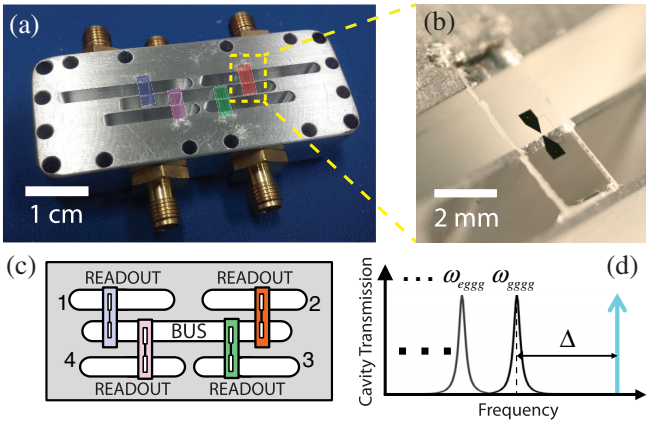


FIG. 1. (a) Picture of our superconducting 4-qubit 3D cQED system with 5 cavities. Four single-qubit chips (false colored: red, blue, green, and pink) are mounted to couple to the bus cavity (center pocket) and individual readout cavities (outer pockets). (b) Close-up photograph of a 3D qubit chip. (c) Diagram of the 4-qubit 3D cQED system. (d) The microwave drive for the RIP gate (cyan arrow) is blue detuned by frequency Δ from the dressed cavity resonance $\omega_{gggg}$. Here, $g$ and $e$ indicate the ground and excited states of a qubit.

 

TABLE I. Parameters of the two 4-qubit devices, device A and device B. $\omega_q$ is the qubit frequency, $\delta$ is the qubit anharmonicity, $\chi$ is the qubit-bus dispersive frequency shift, $\omega_c$ is the readout cavity frequency, $T_1$ is the energy decay time of the qubit, $T_2^*$ is the Ramsey coherence time, and $T_{\text{echo}}$ is the Hahn echo time. Values of $T_1$, $T_{\text{echo}}$, and $T_2^*$ were measured multiple times throughout the experiments and are listed as a range in the table. The bus cavity frequencies are 6.9676 GHz (device A) and 6.9710 GHz (device B). In both cases, the bus cavity has a decay rate $\kappa/2\pi = 7.7$ kHz.

| Qubit index | $\omega_q/2\pi$ (GHz) | $\delta/2\pi$ (MHz) | $\chi/2\pi$ (MHz) | $\omega_c/2\pi$ (GHz) | $T_1$ ($\mu$s) | $T_{\text{echo}}$ ($\mu$s) | $T_2^*$ ($\mu$s) | Qubit index | $\omega_q/2\pi$ (GHz) | $\delta/2\pi$ (MHz) | $\chi/2\pi$ (MHz) | $\omega_c/2\pi$ (GHz) | $T_1$ ($\mu$s) | $T_{\text{echo}}$ ($\mu$s) | $T_2^*$ ($\mu$s) |
|---|---|---|---|---|---|---|---|---|---|---|---|---|---|---|---|
| $A1$ | 5.7862 | 305 | 10 | 10.2020 | 26–36 | 36–40 | 6–17 | $B1$ | 5.7828 | 303 | 6.8 | 10.1949 | 31–36 | 30–40 | 27 |
| $A2$ | 5.1459 | 304 | 3.7 | 10.0846 | 63–68 | 49–68 | 21–23 | $B2$ | 4.5597 | 287 | 0.7 | 10.0805 | 88–90 | 46–86 | 48 |
| $A3$ | 6.3037 | 243 | 4.6 | 9.9799 | 45–59 | 22–34 | 12–42 | $B3$ | 6.3657 | 234 | 6.7 | 9.9775 | 46–59 | 16–27 | 12 |
| $A4$ | 4.7630 | 280 | 2.2 | 9.8328 | 56–68 | 45–46 | 37 | $B4$ | 4.9624 | 284 | 0.1 | 9.8553 | 38–45 | 33–36 | 18 |

we demonstrate the frequency flexibility by performing the RIP gate between 12 individual qubit pairs from two devices, with qubit-qubit detunings up to 1.8 GHz. High-fidelity CZ gates are observed in pair subspaces using 2-qubit randomized benchmarking (RB). Finally, using pairwise CZ interactions in the 4-qubit subspace, we generate a 4-qubit Greenberger-Horne-Zeilinger (GHZ) state.

Figure 1(a) shows our 4-qubit 3D cQED device. The qubits are fabricated on heat exchanger method (HEM) sapphire substrates [20], diced into individual $2 \times 6$ mm$^2$ chips [Fig. 1(b)], mounted in a 5-cavity enclosure machined from 6061 aluminum. Our device is optimized for the best performance of RIP gates between all qubit pairs. The optimization is done by selecting individual qubit chips for

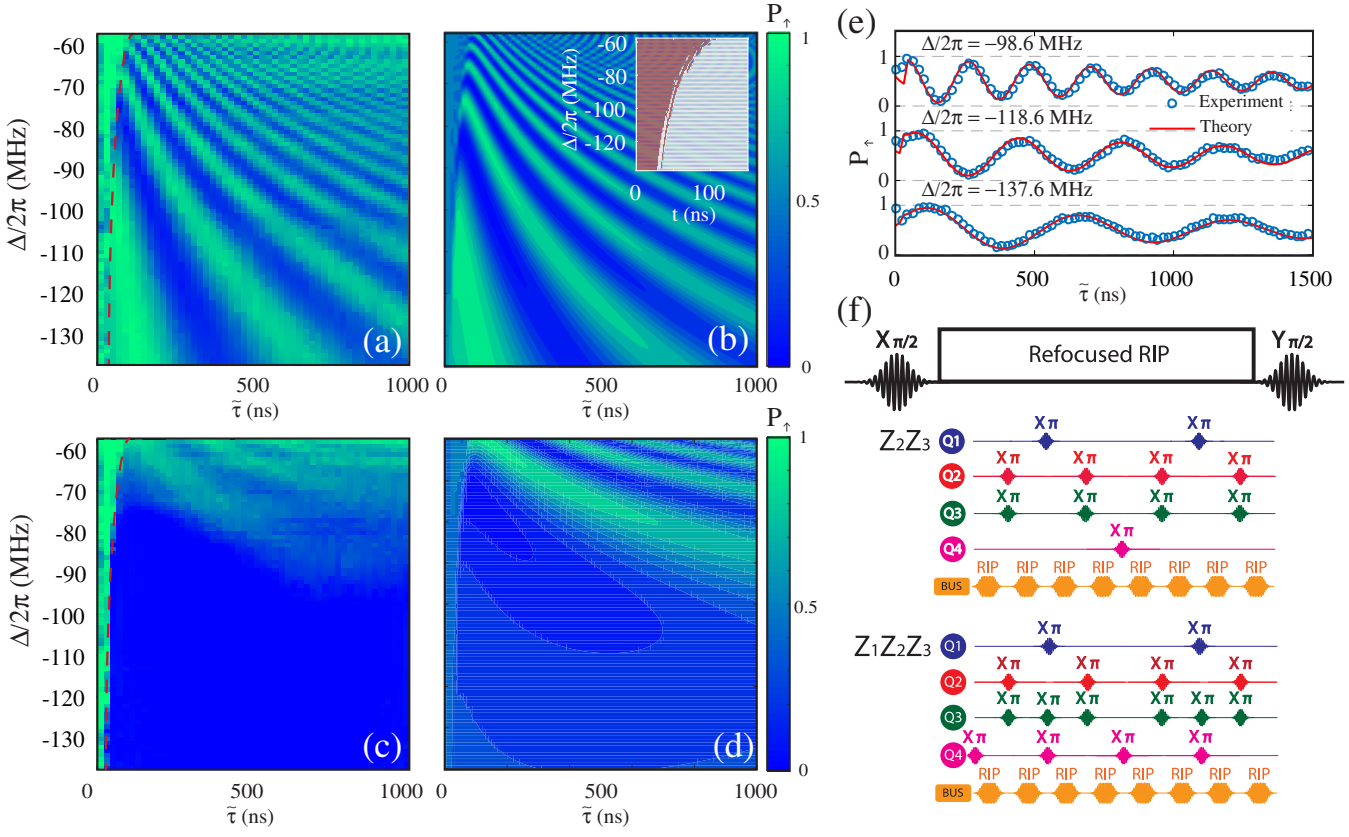


FIG. 2. (a) Excited state population ($P_\uparrow$) of the qubit $A2$ (see Table I) versus single RIP pulse gate time $\tilde{\tau}$ and detuning $\Delta/2\pi$, from Ramsey experiments for $Z_2Z_3$ shown in (f). The red dashed line indicates a threshold time below which no coherent oscillation is observed. (b) Theoretical prediction of $ZZ$ oscillations at $\tilde{\epsilon}_R/2\pi = 315$ MHz. Inset: Simulated residual photons $\langle n(\tilde{\tau})\rangle$ vs $\tilde{\tau}$ and $\Delta/2\pi$. The red region indicates $\langle n(\tilde{\tau})\rangle > 0.01$; $\langle n(\tilde{\tau})\rangle$ drops sharply after the threshold time. (c) $P_\uparrow$ of $A1$ for $Z_1Z_2Z_3$ in (f), showing $ZZZ$ interactions among qubits $A1$, $A2$, and $A3$ as a function of $\tilde{\tau}$. (d) Theoretical calculation of $ZZZ$ oscillations at $\tilde{\epsilon}_R/2\pi = 200$ MHz. (e) $P_\uparrow$ of $A2$ vs $\tilde{\tau}$ at three detuning points. $ZZ$ oscillations from the experiment (blue circles) and theory (red curves) show good agreement. The theoretical drive amplitude is fine-tuned at $\tilde{\epsilon}_R/2\pi = 315 \pm 15$ MHz. (f) Illustration of the pulse sequences for the Ramsey experiment (top) and 4-qubit refocused RIP gate schemes for $Z_2Z_3$ (middle) or $Z_1Z_2Z_3$ (bottom).

frequency and coherence times. The parameters of the two 4-qubit devices (device A and device B) are listed in Table I. Experimental setups are described in Ref. [21]. The qubit states are measured via low-power dispersive readout [24]. The single-qubit and simultaneous RB results show that all single-qubit gate fidelities are higher than 0.999 [21], confirming no significant addressability errors [25].

The RIP gate is operated by applying a microwave drive detuned by $\Delta$ to the bus [see Fig. 1(d)]. During this operation, the bus cavity evolves adiabatically from its initial vacuum state, back to the vacuum at the end of the gate, and each state of the qubits acquires a state-dependent phase, due to a dispersive shift that leads to a different detuning from the drive frequency. These phases enable the gate to act as controlled-Z (CZ) gate, making the gate insensitive to phase fluctuations in the drive [21].

The action of the RIP gate is described by a sum of Duffing oscillator Hamiltonians coupled to the bus cavity [21]. A large frequency difference between the qubits and the bus cavity results in qubit-qubit photon exchanges. When the qubit frequencies are sufficiently spaced, the qubit-qubit exchanges become state-dependent shifts, with a static contribution and a dynamical one activated by the cavity drive. In general, the gate activates many-body Pauli interactions of different weight, i.e., operators with different numbers of Pauli terms. In our system, Pauli interactions of weight two, $\exp[i\dot{\theta}_{Z_iZ_j}Z_iZ_jt]$, three, $\exp[i\dot{\theta}_{Z_iZ_jZ_k}Z_iZ_jZ_kt]$, and four, $\exp[i\dot{\theta}_{Z_1Z_2Z_3Z_4}Z_1Z_2Z_3Z_4t]$, occur. The interaction rates depend on the state-dependent dispersive shifts, the drive amplitude $\tilde{\epsilon}$, and $\Delta$. With an unmodulated drive, the steady-state rates scale as $\dot{\theta}_{Z_iZ_j} \propto \bar{n}\chi/\Delta$, $\dot{\theta}_{Z_iZ_jZ_k} = \dot{\theta}_{Z_iZ_j}\chi/\Delta$, and $\dot{\theta}_{Z_1Z_2Z_3Z_4} = \dot{\theta}_{Z_iZ_j}(\chi/\Delta)^2$, where $\bar{n} = (|\tilde{\epsilon}|/2\Delta)^2$ is the average number of photons in the bus and $\chi$ is the state-dependent dispersive shift to the bus. Since typically $\chi$ is much smaller than $\Delta$, the interaction rate slows down by $\chi/\Delta$ as the weight of the interaction increases.

To observe the amplitude- and frequency-scaling behavior of the phases from weight two and three $Z$ operators, we perform a series of Ramsey experiments while applying the RIP gate. Refocused RIP gate schemes are designed for 4 qubits to single out $ZZ$ or $ZZZ$ terms. The pulse sequences are shown in Fig. 2(f). In the refocused RIP gate scheme, $X_\pi$ pulses on each qubit are applied between RIP gate pulses, and echo away unwanted $Z$ interactions of various Pauli weights. The sign of the phase of the interaction term $Z_2Z_3$ remains the same along the whole echo sequence, whereas all other $Z_i$, $Z_iZ_j$, $Z_iZ_jZ_k$ and $Z_1Z_2Z_3Z_4$ terms alternate sign along the sequence, resulting in no net phase accumulation. The RIP gate pulse is shaped in the form $\tilde{\epsilon}_R(t) = \tilde{\epsilon}_A\{1 + \cos[\pi\cos(\pi t/\tilde{\tau})]\}$ [26], where $\tilde{\tau}$ is the pulse width. This pulse shape suppresses the photon population of the cavity to third order in $\Delta$, having zero time derivative up to the third order, at the beginning and the end of the pulse [17].

Two-qubit interactions ($Z_2Z_3$) between qubits $A2$ and $A3$, and three-qubit interactions ($Z_1Z_2Z_3$) between qubits $A1$, $A2$, and $A3$ from device A are shown in Figs. 2(a) and 2(c), respectively, as a function of a single RIP gate pulse width $\tilde{\tau}$ and $\Delta$. Both $Z_2Z_3$ and $Z_1Z_2Z_3$ become faster as $\Delta$ approaches zero, as predicted by the steady-state rates. The experimental $Z_2Z_3$ and $Z_1Z_2Z_3$ are compared with a closed-form solution for the density matrix of the system [21]. We find excellent agreement between the experiment [Figs. 2(a) and 2(c)] and theory [Figs. 2(b) and 2(d)], observing deviations of ~0.5% in the pulse amplitude for the different drive detunings. Figure 2(e) shows $Z_2Z_3$ from three different drive detunings. The deviations are likely related to cavity nonlinearity and frequency-dependent attenuation of the drive lines.

In our experiment, the rise time of the RIP gate pulse shortens as the pulse width decreases in $\tilde{\epsilon}_R(t)$. As a result, both the experiment and theory in Fig. 2 reveal a threshold time, below which the gate is strongly inhibited due to nonadiabatic driving. A fast rise of the RIP gate pulse is signaled by the presence of residual photons in the bus at the end of the gate. The nonadiabatic time threshold is marked with a red dashed line in Figs. 2(a) and 2(c) and is inversely proportional to $\Delta$. The closed-form solutions [21] indicate a finite amount of residual photons $\langle n(\tilde{\tau})\rangle > 0.01$ for short gate times, as plotted as the red region in the inset of Fig. 2(b).

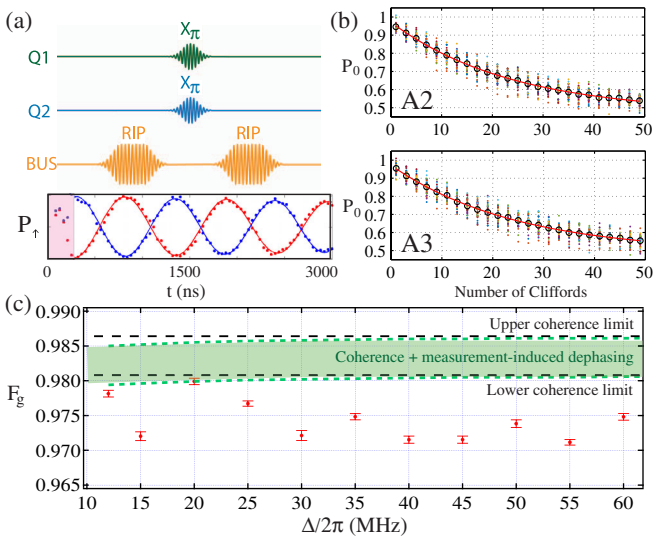


FIG. 3. (a) Pulse sequence of the 2-qubit refocused RIP gate scheme and $P_\uparrow$ of a target qubit from a tune-up procedure using a Ramsey experiment when a control qubit is in the ground state (blue) and in the excited state (red). (b) Population of $|0\rangle$ versus the number of Cliffords from the 2-qubit RB on $A2$-$A3$ at $\Delta/2\pi = 20$ MHz with 40 randomization sequences (colored dots). (c) $ZZ_{\pi/2}$ fidelity between $A2$-$A3$ vs $\Delta/2\pi$ (red dots). The error bars are from the 2-qubit RB fit. Theoretical upper and lower limits on the gate fidelity without (black dashed line) and with the measurement-induced dephasing (green region, dashed curves) are calculated from minimum and maximum coherence times in Table I.

TABLE II. RIP gate fidelities measured on 12 different qubit pairs in devices A and B with $\Delta/2\pi = 40$ MHz. $\Delta_q$ is the detuning between control and target qubits, $T_{\text{gate}}$ is the total refocused gate time shown in Fig. 3, $\zeta$ is the rate of static $ZZ$ interaction, $F_{\text{coh}}$ is the coherence limit on the gate fidelity with the worst $T_1$ and $T_{\text{echo}}$, $F_C$ is the fidelity per Clifford from the 2-qubit RB, and $F_g$ is the fidelity per CZ generator from the average number ($N_C$) of generators per Clifford.

| $\Delta_q/2\pi$ (GHz) | Qubit pair | $T_{\text{gate}}$ (ns) | $\zeta/2\pi$ (kHz) | $F_{\text{coh}}$ | $F_C$ | $F_g$ |
|---|---|---|---|---|---|---|
| 0.383 | *A2*-*A4* | 525 | 60 | 0.9893 | 0.9577(6) | 0.9787(3) |
| 0.403 | *B2*-*B4* | 760 | 10 | 0.9832 | 0.9320(12) | 0.9655(6) |
| 0.518 | *A1*-*A3* | 285 | 138 | 0.9913 | 0.9665(9) | 0.9831(4) |
| 0.583 | *B1*-*B3* | 472 | 156 | 0.9772 | 0.9554(6) | 0.9775(3) |
| 0.637 | *A1*-*A2* | 285 | 107 | 0.9883 | 0.9683(9) | 0.9841(4) |
| 0.820 | *B4*-*B1* | 472 | 34 | 0.9827 | 0.9501(7) | 0.9748(4) |
| 1.023 | *A4*-*A1* | 461 | 60 | 0.9857 | 0.9532(8) | 0.9764(4) |
| 1.158 | *A2*-*A3* | 413 | 60 | 0.9861 | 0.9709(7) | 0.9853(3) |
| 1.223 | *B1*-*B2* | 424 | 16 | 0.9872 | 0.9651(7) | 0.9825(3) |
| 1.403 | *B3*-*B4* | 424 | 10 | 0.9805 | 0.9486(4) | 0.9741(2) |
| 1.541 | *A3*-*A4* | 509 | 30 | 0.9824 | 0.9674(6) | 0.9836(3) |
| 1.806 | *B2*-*B3* | 424 | 23 | 0.9831 | 0.9670(6) | 0.9834(3) |

To demonstrate the flexibility of the RIP gate with respect to qubit frequencies, we characterize the gate performance via 2-qubit RB [7,27] over a large range of qubit-qubit detuning $\Delta_q$. For the characterization, we restrict our experiment to a 2-qubit subspace with the other two qubits in the ground state. The 2-qubit refocused RIP gate scheme [28] [Fig. 3(a)] is used to realize a 2-qubit CZ generator $ZZ_{\pi/2} = \exp[-i(\pi/4)ZZ]$. The gate is tuned up using Ramsey experiments, shown in Fig. 2(f), by performing first a $X_{\pi/2}$ gate on the target qubit, then applying the refocused RIP gate with a varying gate time. The final $Y_{\pi/2}$ on the target qubit ensures, when the phase of the target qubit is $\pm\pi/2$, a maximal contrast between two Ramsey curves for each control qubit state. The lower plot in Fig. 3(a) shows two out-of-phase Ramsey curves as a function of gate time from a tune-up procedure. In the tune-up, the minimum gate time is typically bounded by the nonadiabatic time threshold, which is highlighted in pink in Fig. 3(a).

An example of 2-qubit RB results is shown in Fig. 3(b). We fit the 2-qubit RB result from each qubit to the decay model from Ref. [7,27] to obtain the base ($\alpha$) of the exponential decay model, from which we extract the fidelity per two-qubit Clifford ($F_C$), assuming perfect single-qubit gates. The fidelity per CZ gate ($F_g$) is then computed using the average number of CZ generators per Clifford ($N_C$) with the formula $F_g = 1 - (d-1)(1-\alpha^{1/N_C})/d$, where $d = 4$ is the dimension of the 2-qubit computational space and $N_C = 1.5$. A pair of fidelity data is obtained from two decay curves in one RB run. The data shown in Fig. 3(b) and Table II are an average of the pair.

High-fidelity $ZZ_{\pi/2}$ interactions are achieved by the RIP gate between all qubit pairs, up to 1.8 GHz in $\Delta_q$ (see Table II). The fidelity data are summarized in Table II. The fidelity per Clifford ranges from 0.93 to 0.97, corresponding to 0.96–0.98 fidelity per CZ generator (see Table II caption). The measurement-induced dephasing is a source of error, caused by the photons from the RIP gate that are entangled with qubits and leak out with qubit information [18]. However, we find that the effect of measurement-induced dephasing [29] is small in our devices. The measurement-induced dephasing is investigated by measuring the gate fidelity while varying the detuning of the RIP gate drive between $A2$ and $A3$, as shown in Fig. 3(c). The measurement-induced dephasing is expected to worsen as the detuning decreases. The RIP gate

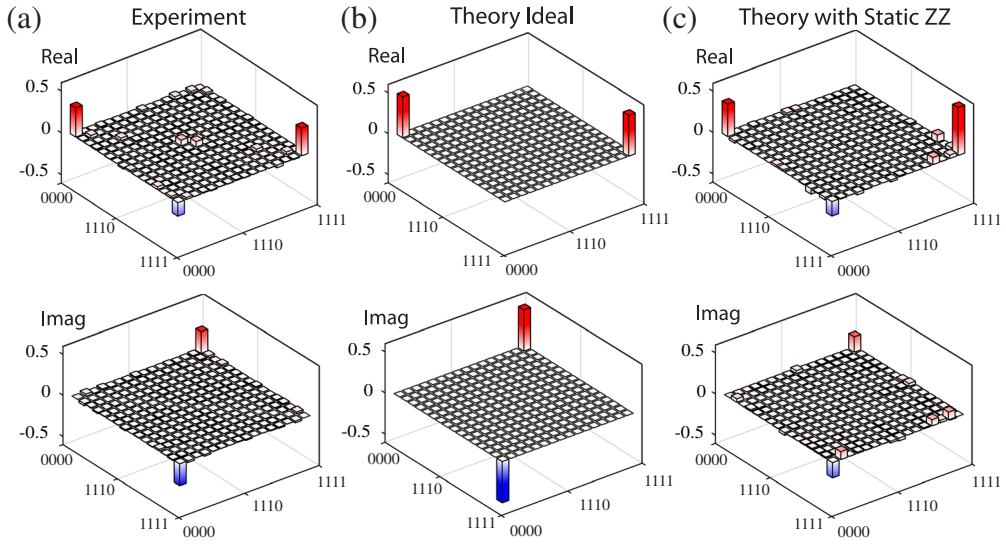


FIG. 4. (a) Experimentally reconstructed density matrix of a 4-qubit GHZ state from the quantum state tomography [30] performed on device A. The 4-qubit refocused RIP gate scheme is used to create the GHZ state. (b) Theoretically reconstructed ideal density matrix of a 4-qubit GHZ state using the exact gate sequences from the experiment in (a). (c) Theoretical density matrix with static $ZZ$ interactions.

pulse width is fixed at 266.7 ns (total refocused RIP gate time is 570 ns), and we keep the gate time constant by adjusting the drive amplitude for all drive detuning. At the 20 MHz detuning, the fidelity per Clifford is 0.9709(7), corresponding to 0.9853(3) for the fidelity per CZ generator, which is close to the lower fidelity bound imposed by the coherence times and the measurement-induced dephasing. We find no appreciable dependence on the detuning of the RIP drive down to 12 MHz, and below 12 MHz the gate does not work due to nonadiabaticity. The overall RIP gate fidelity (∼0.97) is close to the coherence limit (0.980–0.985), and the estimated error from the measurement-induced dephasing is about $10^{-3}$ at the lowest detuning of 12 MHz.

Finally, we implement 4-qubit refocused RIP gate schemes [Fig. 2(f)] to perform pairwise CZ gates in the 4-qubit space [21]. Using the 4-qubit refocused schemes, we generate a maximally entangled 4-qubit GHZ state $[|\Psi\rangle = 1/\sqrt{2}(|0000\rangle - i|1111\rangle)]$ in device A using CZ gates between the qubit pairs $A1$-$A2$, $A2$-$A3$, and $A3$-$A4$. Single RIP pulse widths are 203 ns for $A1$-$A2$ and $A2$-$A3$, and 173 ns for $A3$-$A4$, which makes the total CZ gate times to be 1.871 $\mu$s for $A1$-$A2$ and $A2$-$A3$ and 1.631 $\mu$s for $A3$-$A4$ with the single-qubit pulse width of 36.7 ns. The resulting GHZ density matrix is shown in Fig. 4(a). The state fidelity to the ideal GHZ state [Fig. 4(b)] is 60.5% with a maximum likelihood estimation, which is partly limited by decoherence during the long gate, and imperfect tuning of the 4-qubit refocused RIP gate scheme. We find that static $ZZ$ interactions can model some of the nonideality observed in the experiment, reproducing erroneous components in the density matrix [Fig. 4(c)].

In summary, we have implemented the RIP gate in 4-qubit superconducting 3D cQED systems. The RIP gate induces $ZZ$ interactions, which are insensitive to phase fluctuations in the drive, easing requirements on phase stability for the qubit microwave controls. We have characterized 12 2-qubit CZ gates amongst a wide range of qubit frequency detunings, spanning up to 1.8 GHz, and demonstrated high fidelity. This flexibility in qubit frequencies and the demonstrated high fidelity make the RIP gate an attractive tool for quantum operations in a large-scale architecture.

We thank Easwar Magesan, Jim Rozen, and Sarah Sheldon for experimental discussions and Markus Brink, George Keefe, and Mary Beth Rothwell for device fabrication. We acknowledge support from IARPA under Contract No. W911NF-10-1-0324.

H. P., A. M., and M. S. contributed equally to this work.

*hanhee.paik@us.ibm.com

[1] J. Kelly *et al.*, Nature (London) **519**, 66 (2015).
[2] D. Risté, S. Poletto, M.-Z. Huang, A. Bruno, V. Vesterinen, O.-P. Saira, and L. DiCarlo, Nat. Commun. **6**, 6983 (2015).
[3] A. D. Córcoles, E. Magesan, S. J. Srinivasan, A. W. Cross, M. Steffen, J. M. Gambetta, and J. M. Chow, Nat. Commun. **6**, 6979 (2015).
[4] S. Sheldon, L. S. Bishop, E. Magesan, S. Filipp, J. M. Chow, and J. M. Gambetta, Phys. Rev. A **93**, 012301 (2016).
[5] R. Barends *et al.*, Nature (London) **508**, 500 (2014).
[6] S. Sheldon, E. Magesan, J. M. Chow, and J. M. Gambetta, Phys. Rev. A **93**, 060302 (2016).
[7] A. D. Córcoles, J. M. Gambetta, J. M. Chow, J. A. Smolin, M. Ware, J. Strand, B. L. T. Plourde, and M. Steffen, Phys. Rev. A **87**, 030301 (2013).
[8] S. B. Bravyi and A. Yu. Kitaev, arXiv:quant-ph/9811052.
[9] A. G. Fowler, M. Mariantoni, J. M. Martinis, and A. N. Cleland, Phys. Rev. A **86**, 032324 (2012).
[10] F. W. Strauch, P. R. Johnson, A. J. Dragt, C. J. Lobb, J. R. Anderson, and F. C. Wellstood, Phys. Rev. Lett. **91**, 167005 (2003).
[11] L. DiCarlo *et al.*, Nature (London) **460**, 240 (2009).
[12] G. S. Paraoanu, Phys. Rev. B **74**, 140504(R) (2006).
[13] C. Rigetti and M. Devoret, Phys. Rev. B **81**, 134507 (2010).
[14] J. M. Chow *et al.*, Phys. Rev. Lett. **107**, 080502 (2011).
[15] E. Magesan (unpublished).
[16] M. Takita, A. D. Córcoles, E. Magesan, B. Abdo, M. Brink, A. Cross, J. M. Chow, and J. M. Gambetta, Phys. Rev. Lett. **117**, 210505 (2016).
[17] A. W. Cross and J. M. Gambetta, Phys. Rev. A **91**, 032325 (2015).
[18] S. Puri and A. Blais, Phys. Rev. Lett. **116**, 180501 (2016).
[19] H. Paik *et al.*, Phys. Rev. Lett. **107**, 240501 (2011).
[20] O. Dial, D. T. McClure, S. Poletto, G. A. Keefe, M. B. Rothwell, J. M. Gambetta, D. W. Abraham, J. M. Chow, and M. Steffen, Supercond. Sci. Technol. **29**, 044001 (2016).
[21] See Supplemental Material at http://link.aps.org/supplemental/10.1103/PhysRevLett.117.250502, which includes Refs. [22, 23], for additional details on the experimental setup and a theoretical model of the system.
[22] F. Motzoi, J. M. Gambetta, P. Rebentrost, and F. K. Wilhelm, Phys. Rev. Lett. **103**, 110501 (2009).
[23] J. Koch, T. M. Yu, J. Gambetta, A. A. Houck, D. I. Schuster, J. Majer, A. Blais, M. H. Devoret, S. M. Girvin, and R. J. Schoelkopf, Phys. Rev. A **76**, 042319 (2007).
[24] B. Abdo, F. Schackert, M. Hatridge, C. Rigetti, and M. Devoret, Appl. Phys. Lett. **99**, 162506 (2011).
[25] J. M. Gambetta *et al.*, Phys. Rev. Lett. **109**, 240504 (2012).
[26] S. M. Girvin (unpublished).
[27] E. Magesan, J. M. Gambetta, and J. Emerson, Phys. Rev. Lett. **106**, 180504 (2011).
[28] J. M. Chow, J. M. Gambetta, A. W. Cross, S. T. Merkel, C. Rigetti, and M. Steffen, New J. Phys. **15**, 115012 (2013).
[29] J. Gambetta, A. Blais, D. I. Schuster, A. Wallraff, L. Frunzio, J. Majer, M. H. Devoret, S. M. Girvin, and R. J. Schoelkopf, Phys. Rev. A **74**, 042318 (2006).
[30] C. A. Ryan, B. R. Johnson, J. M. Gambetta, J. M. Chow, M. P. da Silva, O. E. Dial, and T. A. Ohki, Phys. Rev. A **91**, 022118 (2015).